Article:
Zhang, L., Algeo, T.J., Sullivan, N.B. et al. (Accepted: 2026) Testing Early Triassic timescales based on sulfur-isotope cyclostratigraphy. Geological Society of America Bulletin. ISSN: 0016-7606 (In Press)

Figures and captions

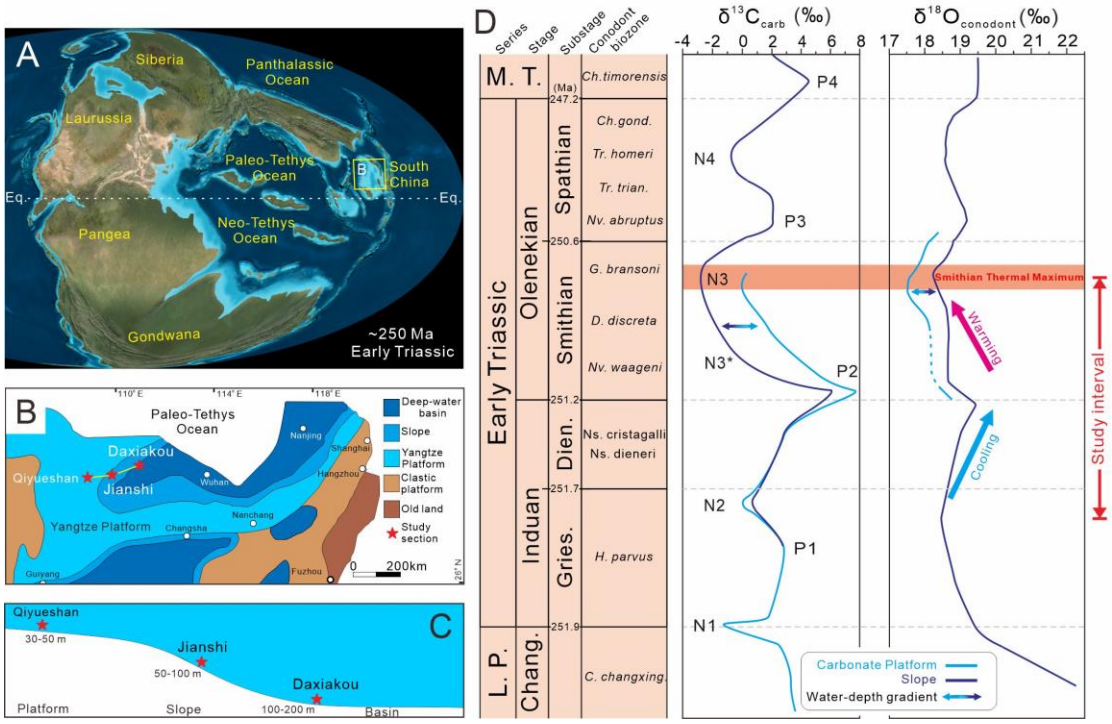

Fig. 1. Paleogeographic maps of (A) the Early Triassic world, (B) South China Craton, and (C) a cross-section of the Yangtze carbonate platform margin, showing the locality of the Qiyueshan, Jianshi and Daxiakou sections. (D) Major perturbations to the marine carbon cycle and climate changes, as revealed from long-term variations in carbonate carbon isotope ($\delta^{13}C_{carb}$) and conodont oxygen isotopes ($\delta^{18}O_{conodont}$), respectively, showing reinforced water-depth gradient especially during the Smithian Thermal Maximum event. In panel C, the schematic cross-section shows estimated paleo-depths (based on facies, not to scale) for the carbonate platform at Qiyueshan, the Jianshi slope section, and the Daxiakou slope-basin transitional setting. In panel D, the $\delta^{13}C_{carb}$ profile is from Payne et al. (2004), and $\delta^{18}O_{conodont}$ profile from Sun et al. (2012). N1 to N4 and P1 to P4 $\delta^{13}C_{carb}$ excursions after Song et al. (2013, 2014). N3* is newly defined in the present study, regarding as an inflection point of the negative excursion from P2 to N3 that is globally comparable (see Fig. 5).

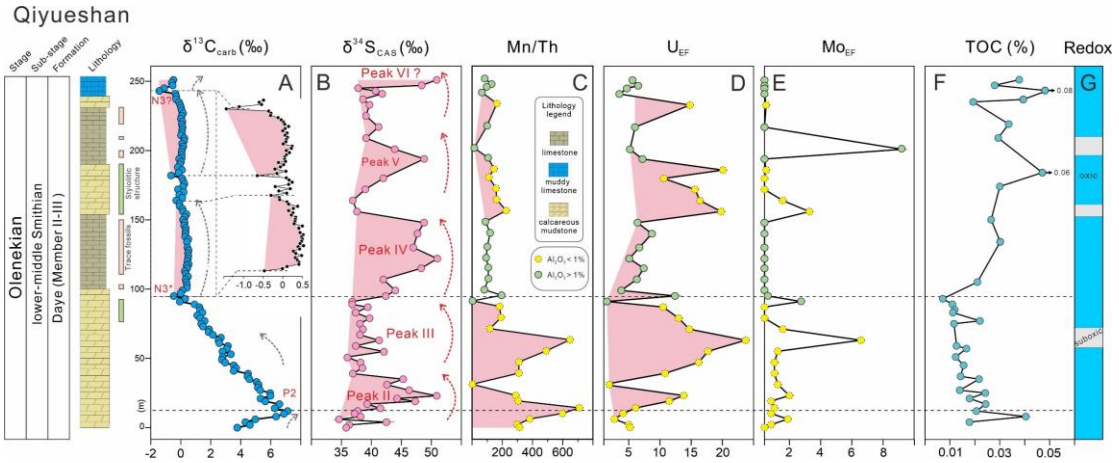

Fig. 2. Geochemical profiles of (A) $\delta^{13}C_{carb}$, (B) $\delta^{34}S_{CAS}$, (C) Mn/Th, (D) U_{EF}, (E) Mo_{EF}, (F) TOC profiles, and (G) local seawater redox conditions for the Qiyueshan section. Ind. = Induan; Dien. = Dienerian. IOB = Induan-Olenekian Boundary. Pink areas show periodic changes in $\delta^{13}C_{carb}$, $\delta^{34}S_{CAS}$, Mn/Th and U_{EF}, indicating cyclicity of marine carbon-sulfur cycles and local seawater redox conditions.

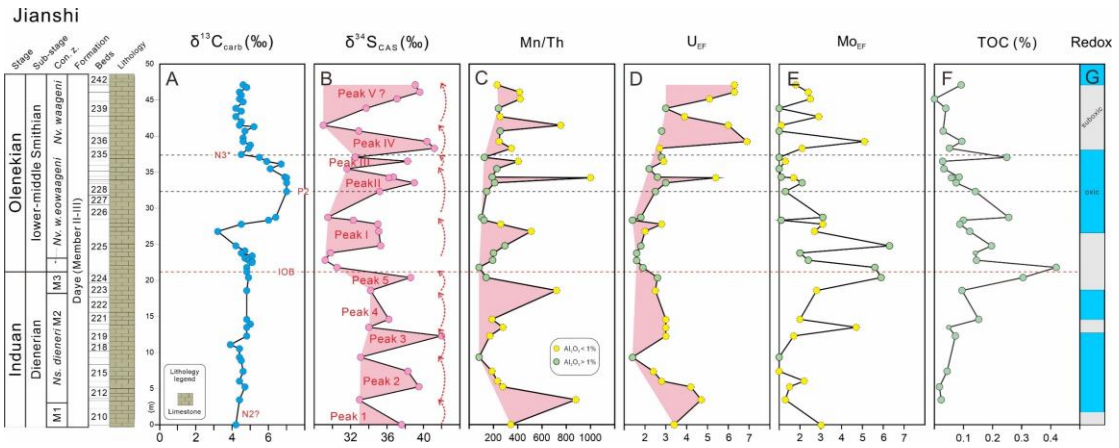

Fig. 3. Geochemical profiles of (A) $\delta^{13}C_{carb}$, (B) $\delta^{34}S_{CAS}$, (C) Mn/Th, (D) U_{EF}, (E) Mo_{EF}, (F) TOC profiles, and (G) local seawater redox conditions for the Jianshi section. Conodont zonations from Lyu et al. (2019). M1 = *Neospathodus dieneri* M1; M3 = *Neospathodus dieneri* M3; *Nv.* = *Novispathodus*; IOB = Induan-Olenekian Boundary.

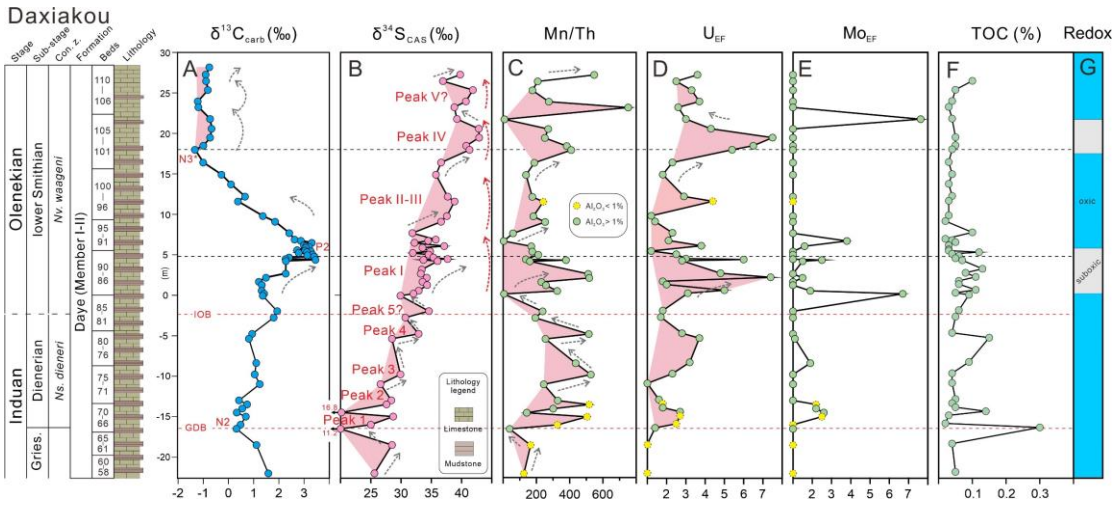

Fig. 4. Geochemical profiles of (A) $\delta^{13}C_{carb}$, (B) $\delta^{34}S_{CAS}$, (C) Mn/Th, (D) U_{EF}, (E) Mo_{EF}, (F) TOC profiles, and (G) local seawater redox conditions for the Daxiakou section. Conodont zonations from Zhao et al. (2013). Gries. = Griesbachian; *Ns*. = *Neospathodus*; *Nv*. = *Novispathodus*; GDB = Griesbachian-Dienerian Boundary; IOB = Induan-Olenekian Boundary.

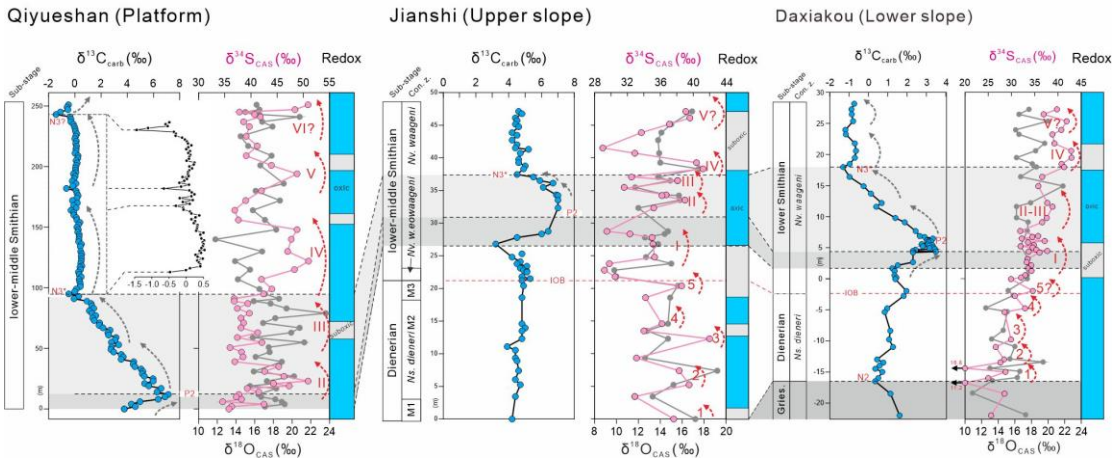

Fig. 5. Compositions of $\delta^{13}C_{carb}$, $\delta^{34}S_{CAS}$ and $\delta^{18}O_{CAS}$ profiles, and local redox conditions in the study sections. Conodont zonation for Jianshi from Lyu et al. (2019), and Daxiakou from Zhao et al. (2013). Six plateau $\delta^{34}S_{CAS}$ values are marked as I to VI that can be correlated among the study sections. Abbreviations refer to Figures 2-4.

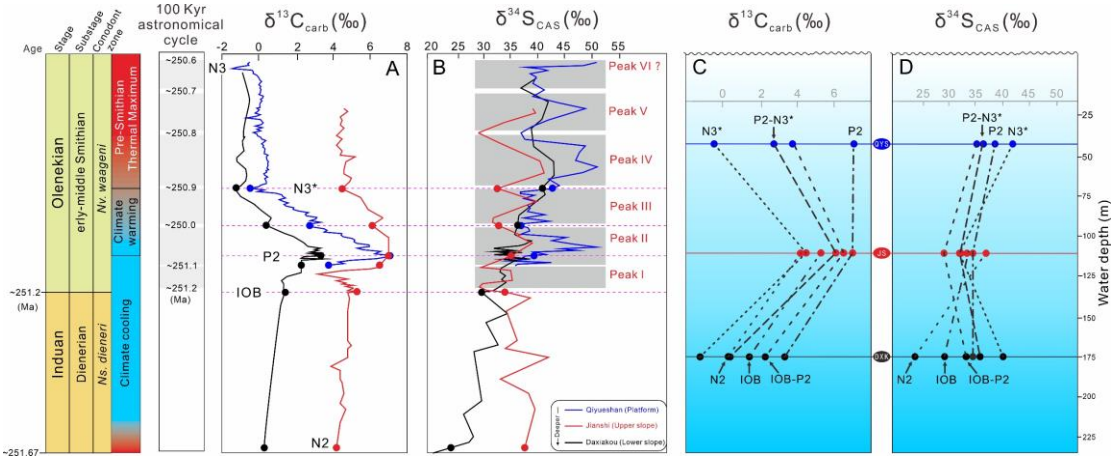

Fig. 6. Compilation of $\delta^{13}C_{carb}$ and $\delta^{34}S_{CAS}$ (A-B), and vertical gradients of $\delta^{13}C_{carb}$ and $\delta^{34}S_{CAS}$ (C-D) from the earliest Dienerian to the middle Smithian. Climate change based on $\delta^{18}O_{conodont}$ variations in Sun et al. (2012).

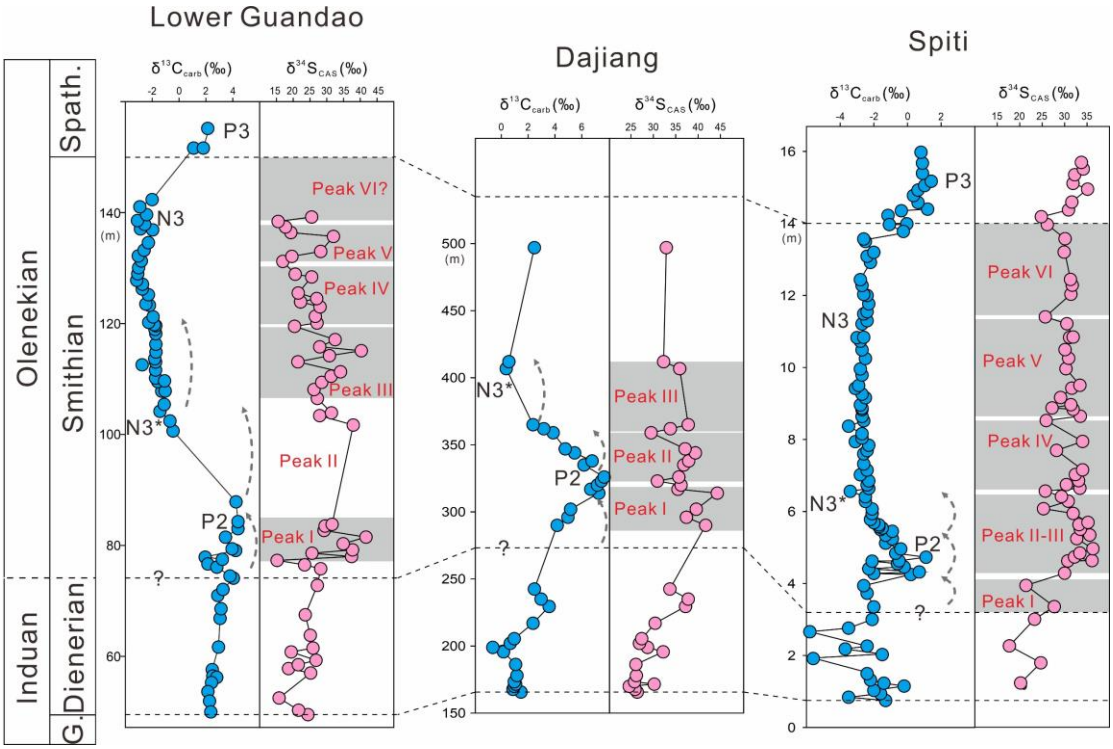

Fig. 7. Geochemical profiles of $\delta^{13}C_{carb}$, $\delta^{34}S_{CAS}$ and [CAS] concentrations in the Lower Guandao and Dajiang (South China) and Spiti (India) sections, showing periodic plateau $\delta^{34}S_{CAS}$ values during the early to middle Smithian. Peak I to VI values besides $\delta^{34}S_{CAS}$ profiles represent six phases of marine sulfur cycle anomaly that can be correlated to other South China sections in the present study. Data sources: Lower Guandao and Dajiang from Song et al. (2014), and Spiti from Stebbins et al. (2019). G. = Griesbachian; Spath. = Spathian.

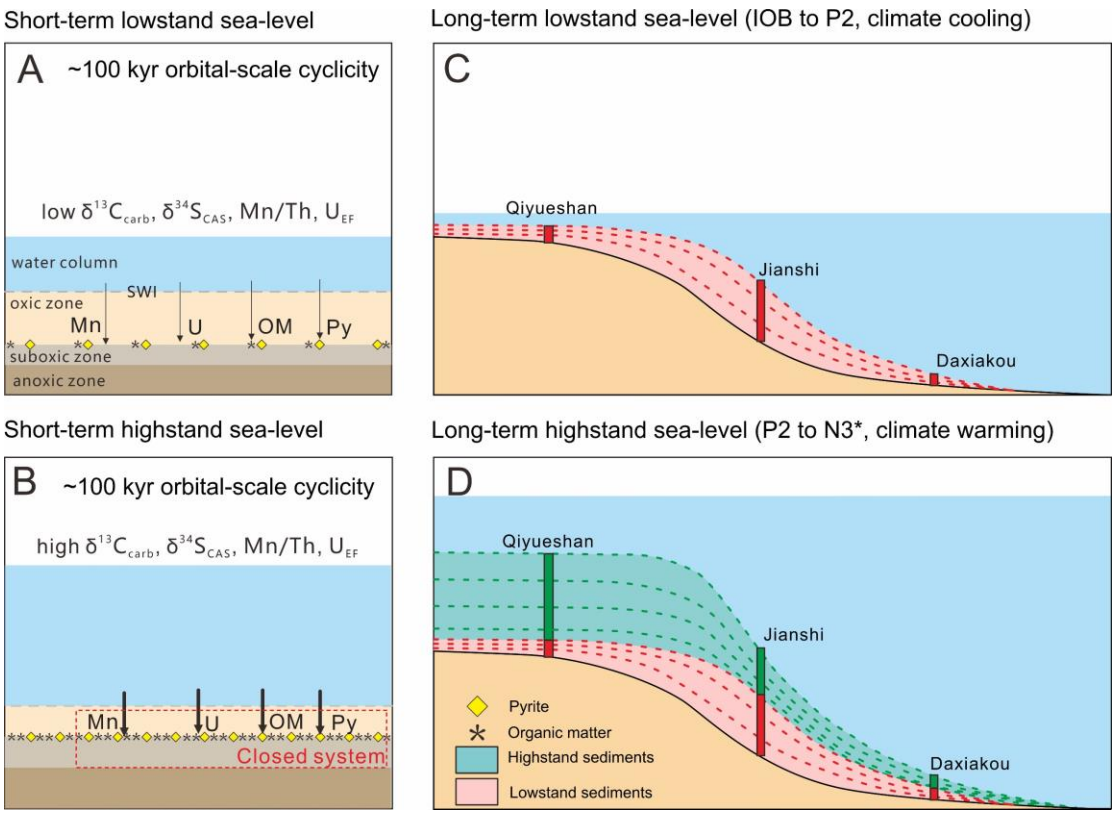

Fig. 8. A cartoon of orbital-scale cyclicity of sea-level changes and long-term 'seesaw' pattern of carbonate sedimentation across the platform-slope area. (A) Low burial rates of redox sensitive elements (i.e., Mn and U), and organic matter and pyrite, causing low $\delta^{13}C_{carb}$, $\delta^{34}S_{CAS}$, Mn/Th and U_{EF} values due to orbital forcing controlled lowstand sea-level; (B) High burial rates of redox sensitive elements (i.e., Mn and U), and organic matter and pyrite, causing high $\delta^{13}C_{carb}$, $\delta^{34}S_{CAS}$, Mn/Th and U_{EF} values (in a closed system) due to orbital forcing controlled highstand sea-level. (C) low sedimentation rate at platform area (e.g., Qiyueshan) versus high sedimentation rate at slope area (e.g., Jianshi) under long-term lowstand sea-level during early Smithian (i.e., IOB to P2) climate cooling. (D) High sedimentation rate at platform area (e.g., Qiyueshan) versus low sedimentation rate at slope area (e.g., Jianshi) under long-term highstand sea-level during early to middle Smithian (i.e., P2 to N3*) climate warming. OM = Organic matter; Py = Pyrite; SWI = Sediment–water interface.

Supplementary figures

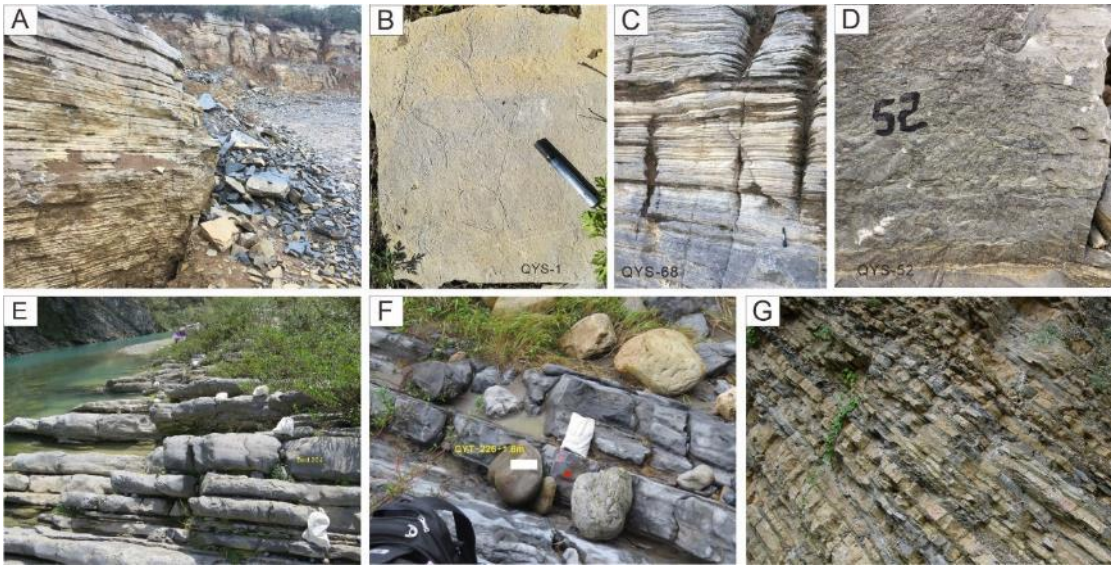

Fig. S1. Field photographs of Qiyueshan (A-D), Jianshi (E-F) and Daxiakou sections (G). (A) output location of (B) ichnoassemblage fossils at the middle part of the section; (C-D) thin-bedded limestone (QYS-68) and intraclastic limestone (QYS-52); (E-F) Thin to intermediate thick limestone that located close to the bottom of a riverbed; (G) interbedded calcareous mudstone and thin-bedded muddy limestone of the upper Dienerian and lower Smithian strata interval (Daye Formation).

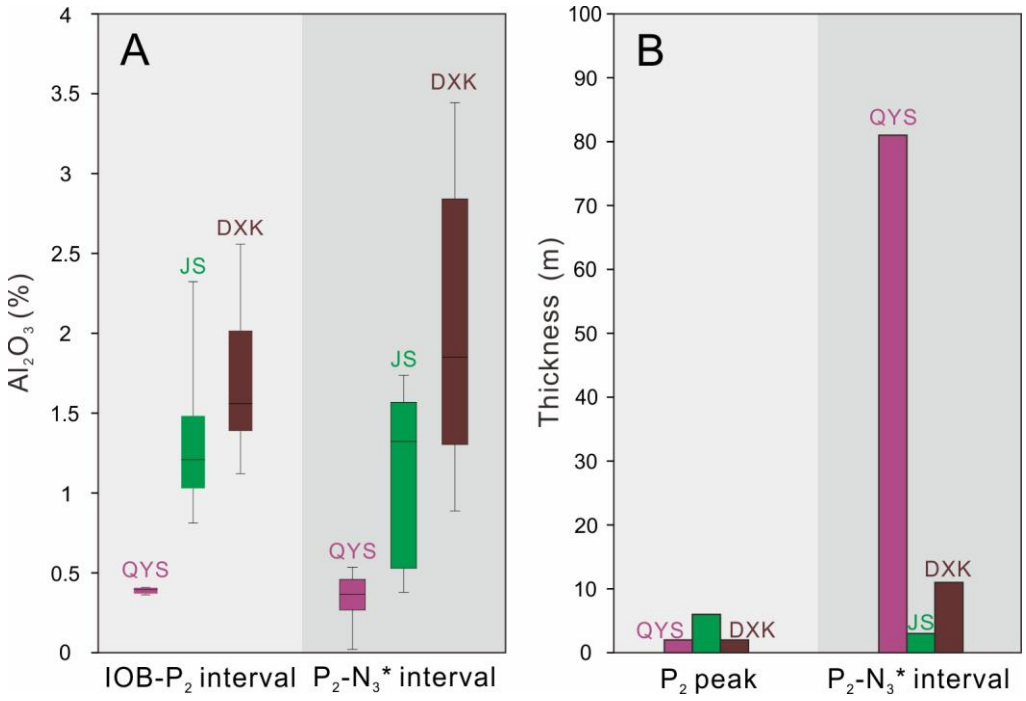

Fig. S2. Comparisons of (A) Al_2O_3 content in carbonate rocks at IOB-P_2 and P_2-N_3* intervals, (B) accumulated thickness and sedimentation rates from GDB to N3, and (C) sedimentary thickness at P_2 excursion and P_2-N_3* intervals among the study sections. GDB = Griesbachian-Dienerian boundary; IOB = Induan-Olenekian boundary. LSR = linear sedimentation rate. P2, N3* and N3

refers to carbon isotopic chemostratigraphy as discussed in the main text.

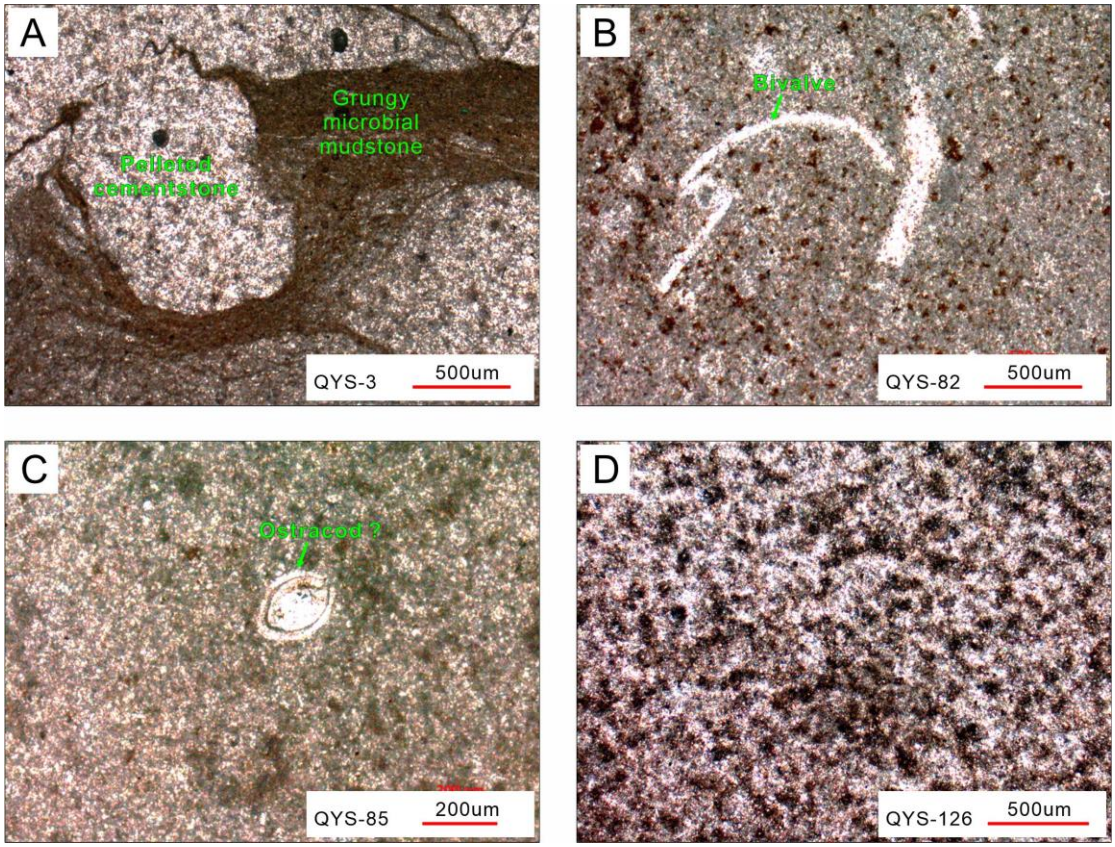

Fig. S3. Thin-section photomicrographs showing typical fossils and clasts in Qiyueshan. (A) mudstone marked by pelleted cementstone surrounded by grungy microbial mudstone; (B) mudstone containing bivalve fragment; (C) mudstone containing a probable ostracod shell; (D) mudstone containing typical pelleted cementstone and microbial aggregates.

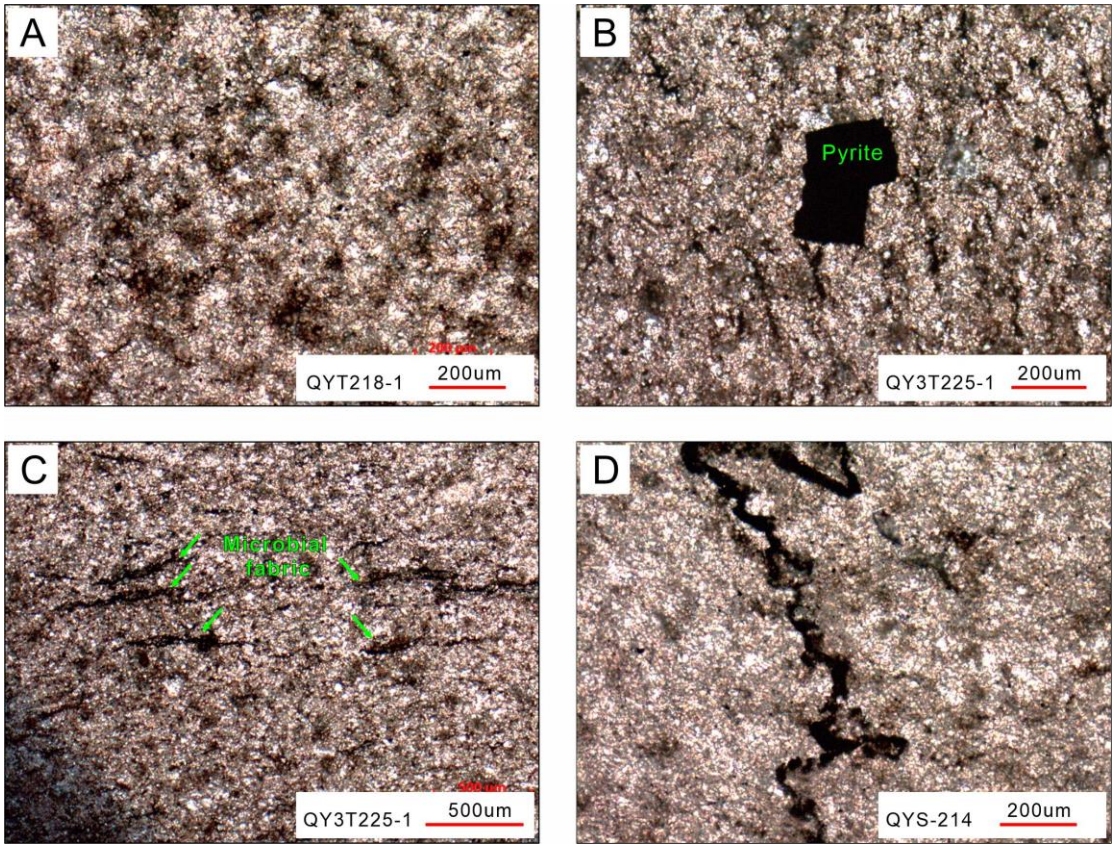

Fig. S4. Thin-section photomicrographs showing typical clasts in Jianshi. (A) mudstone containing typical pelleted cementstone and microbial aggregates; (B-C) mudstone containing pyrite crystals and directionally arranged microbial fabric intermittently interspersed in pelleted cementstone; (D) mudstone containing pelleted cementstone with microbial ribbon.

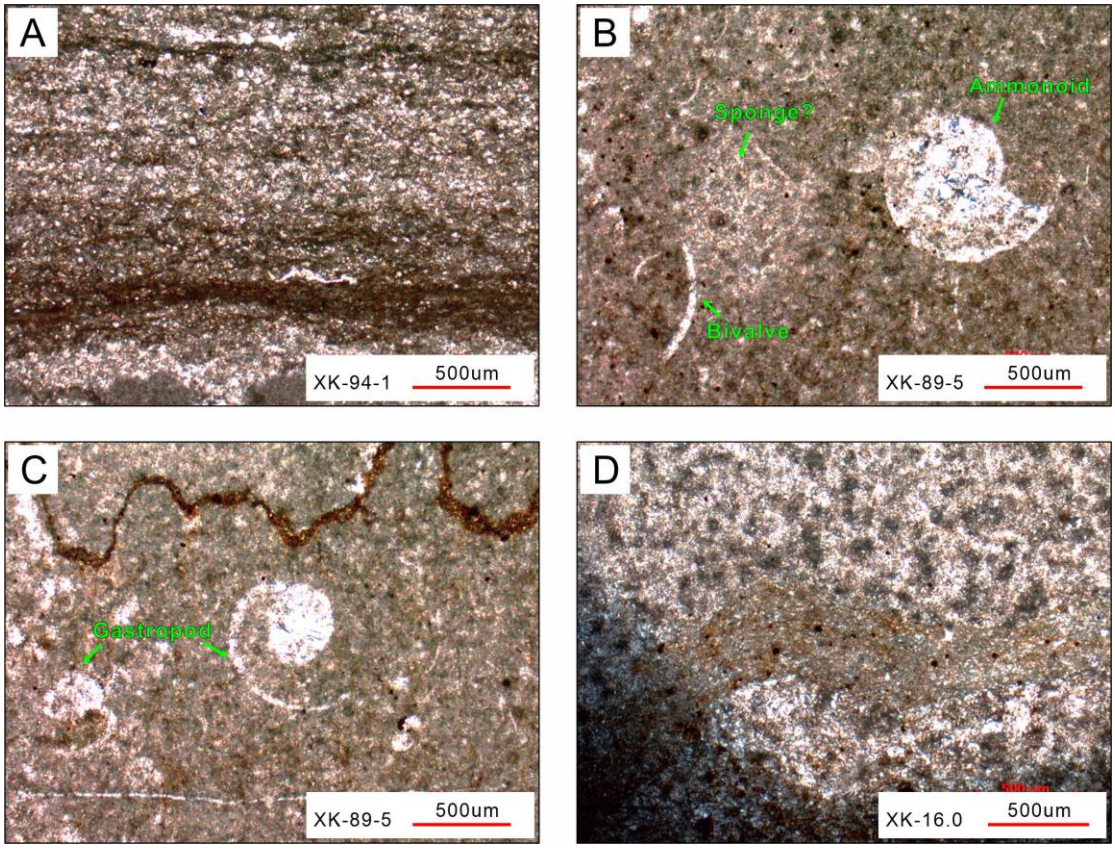

Fig. S5. Thin-section photomicrographs showing typical fossils and clasts in Daxiakou. (A) mudstone containing pelleted cementstone with microbial laminations; (B) mudstone containing ammonoid, bivalve fragment and a probable sponge; (C) mudstone containing gastropod and microbial laminations; (D) mudstone containing typical pelleted cementstone and microbial laminations.

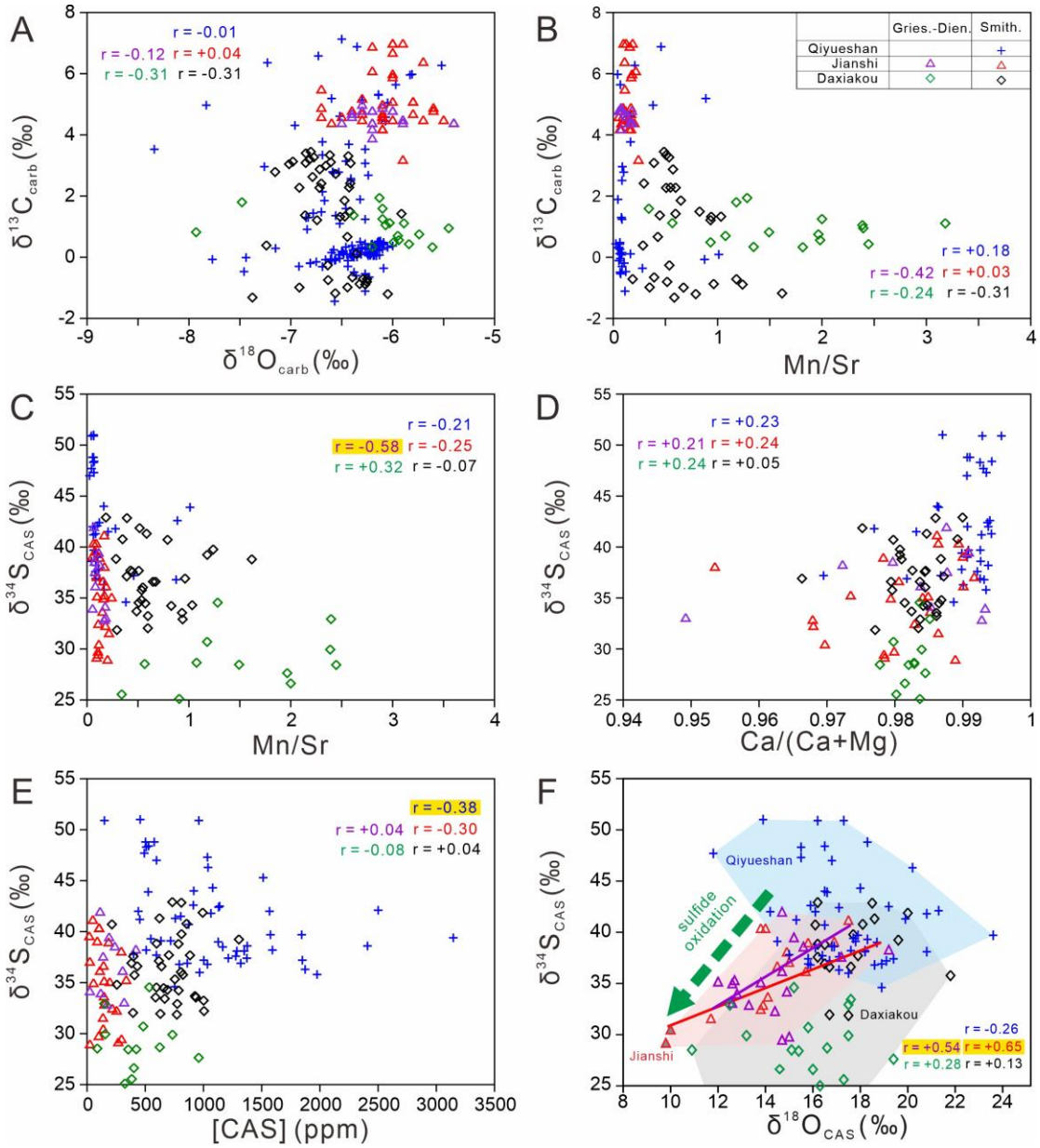

Fig. S6. Correlations between $\delta^{13}C_{carb}$, $\delta^{34}S_{CAS}$, $\delta^{18}O_{CAS}$, $\delta^{18}O_{carb}$, Mn/Sr, Ca/(Ca+Mg) and [CAS] in Qiyueshan, Jianshi and Daxiakou sections. (A) $\delta^{13}C_{carb}$ vs. $\delta^{18}O_{carb}$; (B) $\delta^{13}C_{carb}$ vs. Mn/Sr; (C) $\delta^{34}S_{CAS}$ vs Mn/Sr; (D) $\delta^{34}S_{CAS}$ vs Ca/(Ca+Mg); (E) $\delta^{34}S_{CAS}$ vs [CAS]; (F) $\delta^{34}S_{CAS}$ vs $\delta^{18}O_{CAS}$. Correlation coefficients that statistically significant at $p(\alpha) < 0.05$ are marked in yellow.

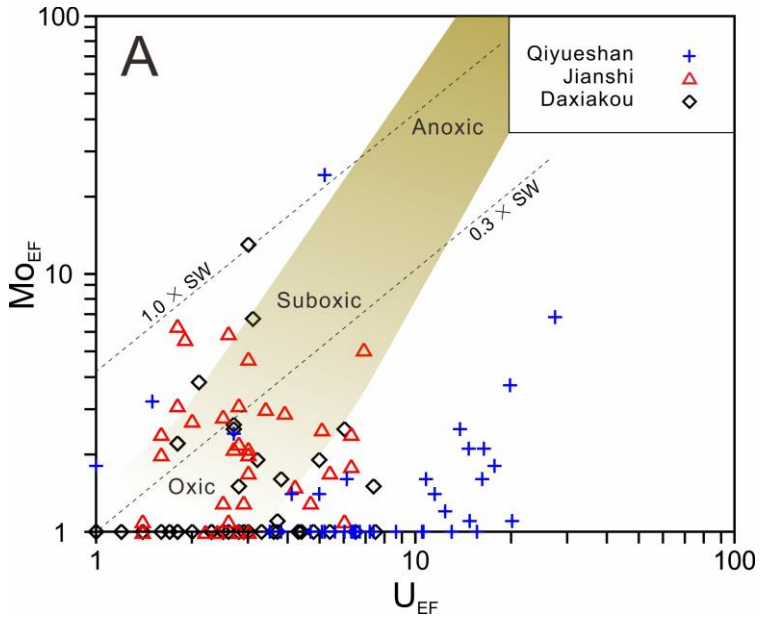

Fig. S7. Crossplots of U_{EF} vs. Mo_{EF} for the study sections.